

See discussions, stats, and author profiles for this publication at: <https://www.researchgate.net/publication/276459137>

Computationally Assisted (Solid-State Density Functional Theory) Structural (X-ray) and Vibrational Spectroscopy (FT-IR, FT-RS, TDs-THz) Characterization of the Cardiovascular Drug...

ARTICLE *in* CRYSTAL GROWTH & DESIGN · MAY 2015

Impact Factor: 4.89 · DOI: 10.1021/acs.cgd.5b00251

CITATION

1

READS

86

7 AUTHORS, INCLUDING:



Jadwiga Mielcarek

Poznan University of Medical Sciences

57 PUBLICATIONS 275 CITATIONS

[SEE PROFILE](#)



Eric Collet

Université de Rennes 1

143 PUBLICATIONS 1,591 CITATIONS

[SEE PROFILE](#)



Aleksandra Pajzderska

Adam Mickiewicz University

45 PUBLICATIONS 141 CITATIONS

[SEE PROFILE](#)

Computationally Assisted (Solid-State Density Functional Theory) Structural (X-ray) and Vibrational Spectroscopy (FT-IR, FT-RS, TDs-THz) Characterization of the Cardiovascular Drug Lacidipine

Kacper Drużbicki,^{*,†,‡} Jadwiga Mielcarek,[§] Anna Kiwilsza,^{†,||} Loic Toupet,[⊥] Eric Collet,[⊥] Aleksandra Pajzderska,[†] and Jan Wąsicki^{†,||}

[†]Department of Radiospectroscopy, Faculty of Physics and ^{||}NanoBioMedical Center, Adam Mickiewicz University, Umultowska 85, 61-614, Poznań, Poland

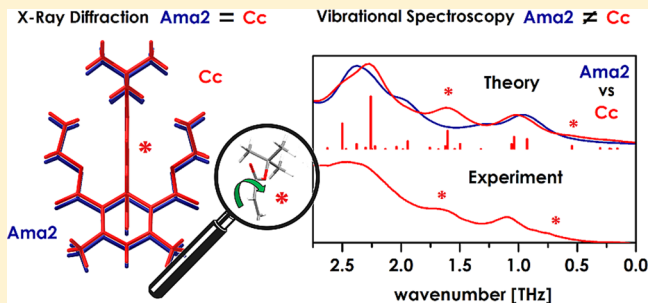
[‡]Frank Laboratory of Neutron Physics, Joint Institute for Nuclear Research, 141980, Dubna, Russian Federation

[§]Department of Inorganic and Analytical Chemistry, Poznań University of Medical Sciences, Grunwaldzka 6, 60-780, Poznań, Poland

[⊥]Institut de Physique de Rennes, UMR CNRS 6251, Université Rennes 1, 35042, Rennes Cedex, France

S Supporting Information

ABSTRACT: The structural properties of a second-generation dihydropyridine calcium antagonist, lacidipine, were explored by combining low-temperature X-ray diffraction with optical vibrational spectroscopy and periodic density functional theory (PBC DFT) calculations. Crystallographic analysis cannot discriminate between two possible molecular symmetries in crystals made of pure lacidipine: the space group *Ama*2, where the lacidipine molecule lies on mirror symmetry, or a *Cc* space group with distorted lacidipine molecules. Intermolecular interactions analysis reveals an infinite net of moderate-strength N–H···O hydrogen-bonds, which link the molecular units toward the crystallographic *b*-axis. Weak interactions were identified, revealing their role in stabilization of the crystal structure. The vibrational dynamics of lacidipine was thoroughly explored by combining infrared and Raman spectroscopy in the middle- and low-wavenumber range. The given interpretation was fully supported by state-of-the-art solid-state density functional theory calculations (plane-wave DFT), giving deep insight into the vibrational response and providing a complex assignment of spectral features. The vibrational analysis was extended onto the lattice-phonon range by employing time-domain terahertz spectroscopy. Analysis of the anisotropic displacement parameters suggests noticeable dynamics of the terminal (*tert*-butoxycarbonyl)vinyl moiety. The terahertz study provides direct experimental evidence of “crankshaft” type motions in the terminal chain. By combining low-wavenumber vibrational spectroscopy with the first-principles calculations, we were able to prove that the quoted thermodynamically stable phase corresponds to the monoclinic *Cc* space group.

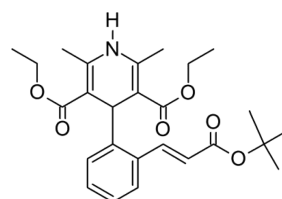


I. INTRODUCTION

Lacidipine (LCDP: diethyl (*E*)-4,2-[(*t*-butoxycarbonyl)vinyl]-phenyl-1,4-dihydro-2,6-dimethylpyridine-3,5-dicarboxylate), with the trade names Caldine, Lacimen, Lacipil, Lacidipil, Lacirex, Midotens, Motens, or Viapres, is a second-generation dihydropyridine calcium antagonist, introduced as a once a day treatment for mild to moderate hypertension (Scheme 1).¹

Because of its high selectivity for vascular smooth muscle, with a long duration of action, it can be used in a wide variety of patients. Therefore, LCDP is an attractive therapy agent for the long-term management of essential hypertension.^{2,3} As with other members of its class, it has shown potentially beneficial anti-atherosclerotic properties by affecting cellular cholesterol metabolism.⁴ In addition, it was suggested that LCDP can protect the patients' kidney cells from apoptosis induced by adenosine triphosphate (ATP) depletion and their recovery by

Scheme 1. Molecular Formula of Lacidipine (LCDP)



regulating the caspase-3 pathway.⁵ Furthermore, LCDP was found to protect stroke-prone hypertensive rats against the impairment of endothelium-dependent vasorelaxation, evoked

Received: February 19, 2015

Revised: May 11, 2015

Published: May 11, 2015

by a salt-rich diet, which may contribute to its beneficial effect against end-organ damage and stroke.⁶ Finally, recent studies have confirmed its significance as an antibacterial and antitoxic compound.^{7,8}

In principle, LCDP is an orally administered agent, having poor bioavailability of approximately 10% due to extensive hepatic metabolism into inactive metabolites.⁹ Lacidipine is a highly lipophilic drug with very low water solubility, which in turn further limits its bioavailability.¹⁰ For that reason, much attention has been already paid to bioavailability enhancement. Recently, we have examined an ordered mesoporous silica material as a potential LCDP nanocarrier.¹¹ A bioavailability enhancement study via microemulsion based transdermal gels was also presented by Gannu et al.,¹² while nanostructured lipid carriers (NLCs) were developed by Anuradha and Kumar.¹³ Alternatively, some novel liposomes were designed for this purpose.¹⁴

According to Raju et al., there are five impurities identified in the lacidipine bulk drug substance, namely, its para-, meta-, and regioisomers along with lacidipine acid and dimer impurities, where the latter one results from the condensation of 2 equiv of *tert*-butoxycarbonylmethyltriphenyl phosphonium bromide with *o*-phthalaldehyde.^{15,16} In addition, in line with the well-known sensitivity of the dihydropyridine family, it was found that LCDP is most sensitive to light and moisture (see Figure S1 in Supporting Information).¹⁷

Light exposure leads to the phototransformation of the trans isomer into the cis analogue, which was first described in ref 18. The study of phototransformation by the artificial sunlight was continued in more detail as an important parameter for drug handling.¹⁹ It was concluded that the ultraviolet-induced transformation pathway leads to drastic intramolecular conversion, resulting in cyclization of LCDP. The final product of the photoconversion was analyzed with X-ray diffraction by Simonic et al.²⁰

Despite the wealth of information gathered about the pharmaceutical activity of LCDP along with its stability and processing, there are, however, no reports focused on the structural or vibrational properties of the title system. Hence, the main motivation of this paper is to fill the void by presenting a complex experimental and theoretical view on the crystal structure, intermolecular interactions, and vibrational spectrum of pure LCDP. Since optical vibrational spectroscopy is the method of choice in active pharmaceutical ingredients (API) studies—including purity and polymorph screening as well as monitoring of the interactions between a drug and a carrier—we have reported detailed vibrational analysis of the title compound. In addition to routinely used infrared and Raman spectroscopy, time-domain terahertz spectroscopy (TDs-THz) has been employed as a method of great potential in both qualitative and quantitative analysis of pharmaceutical solids.²¹ The experimental data were fully interpreted with the help of density functional perturbation theory (DFPT) calculations, which has become the state-of-the-art method for studying vibrational dynamics of condensed matter as pushing the limits of the static quasi-harmonic approach. Sufficient agreement between the theoretical and experimental data was found, providing a possibly thorough assignment of the most prominent spectral features and shedding more light on the influence of the intermolecular interactions on the vibrational dynamics of LCDP.

By combining low-wavenumber vibrational spectroscopy with solid-state DFT calculations, we were able to go beyond

the structural information delivered by X-ray diffraction and illustrate how the quoted methodology can help in revealing the structural features hidden under thermally induced dynamics. Such a combination can be a very powerful tool in revealing the subtle structural differences playing a role in a proper definition of the crystal structures in large and flexible pharmaceutical molecular crystals.

II. EXPERIMENTAL AND COMPUTATIONAL DETAILS

Sample Preparation. Lacidipine sample was kindly provided by BIOFARM pharmaceutical company, Poznan, Poland. It was crystallized from dichloromethane according to the following procedure. A portion of 0.3 g of lacidipine in the form of a white powder was dissolved in 10 mL of dichloromethane and slowly evaporated. It made colorless fine crystals with a melting point at 457–458 K. X-ray diffraction (XRD) measurements of the powder samples were performed in the range of $2\theta = 10\text{--}40^\circ$ (with a step of 0.05°) on a Bruker D8 Advance diffractometer, with a copper anode. The instrument was equipped with a Johansson monochromator working at the wavelength of $\lambda_{\text{Cu}}(K_{\alpha 1}) = 1.5406 \text{ \AA}$.

Single-Crystal X-ray Diffraction. Diffraction measurements were performed at 140 K with an Oxford Diffraction Xcalibur Sapphire 3 CCD single-crystal diffractometer, equipped with a graphite monochromatized Mo $K\alpha$ radiation source. The data collection (Crysalis, 2013)²² ($2\theta_{\text{max}} = 54^\circ$; omega scan frames via 0.7° omega rotation of 20 s per frame, the *HKL* range: $H = -17, 17; K = -28, 29; L = -10, 9$) provided 10 423 reflections. The structure was refined in two possible space groups: *Ama*2 and *Cc*. For the orthorhombic *Ama*2 structure, the collected data result in 2776 independent reflections from which 2324 were found with $I > 2.0\sigma(I)$. The structure was solved with SIR-97,²³ which reveals the non-hydrogen atoms of the molecule. After anisotropic refinement, all hydrogen atoms were found with a Fourier difference. The whole structure was refined with SHELXL97²⁴ by applying the full-matrix least-squares techniques (use of *F* square magnitude; x, y, z, β_{ij} for C, O, and N atoms, x, y, z in riding mode for H atoms; 173 variables with the resulting $R = 0.0413$, $R_w = 0.0908$ and $S_w = 1.059$, $\Delta\rho < 0.16 \text{ e}\cdot\text{\AA}^{-3}$).

For the monoclinic *Cc* structure, the collected data resulted in 4766 independent reflections from which 3837 were found with $I > 2.0\sigma(I)$. The structure was solved in the same way with SIR-97,²³ and refined with SHELXL97²⁴ (299 variables with the resulting $R = 0.0693$, $R_w = 0.0928$ and $S_w = 1.737$, $\Delta\rho < 0.96 \text{ e}\cdot\text{\AA}^{-3}$). The crystallographic data along with the structural refinement parameters for two alternative crystal structures are summarized in Table 1.

The crystallographic data for this paper are deposited at the Cambridge Crystallographic Data Center (CCDC 981400; 1050027). These data can be obtained free of charge via www.ccdc.cam.ac.uk/data_request/cif.

Optical Vibrational Spectroscopy (FT-IR, FT-RS, TDs-THz). All the vibrational spectroscopy measurements were performed for powder samples at room temperature. The middle-FT-IR spectroscopy was applied in a transmission mode, using a Bruker 66v/S FT-IR spectrometer, working with a deuterated triglycine sulfate (DTGS) detector and a silicon carbide (Globar) source. The spectrum was recorded using a KBr pellet, by collecting 64 scans with a spectral resolution of 1 cm^{-1} as covering the range of $4000\text{--}400 \text{ cm}^{-1}$. A far-infrared (FT-FIR) spectrum was collected using a Bruker Vertex v70 vacuum spectrometer, equipped with a polyethylene detector and a Globar source. The sample was suspended in Apiezon N grease and placed on a polyethylene disc. The measurements were done with a spectral resolution of 2 cm^{-1} , by accumulation of 64 scans.

The FT-Raman spectroscopy measurements were performed using a Bruker Raman FRA 106/S module, equipped with a germanium detector and the 1064 nm excitation line of a Nd:YAG laser. The laser power of 350 mW, spectral resolution of 2 cm^{-1} , and accumulation of 2000 scans were chosen as the experimental conditions. The spectrum was recorded down to 50 cm^{-1} .

A time-domain terahertz (TDs-THz) spectroscopy study was performed in the transmission mode, using a Teraview TPS 3000

Table 1. Crystallographic Data and the Structure Refinement Parameters for Lacidipine at 140 K^a

molecular formula	<chem>C26H33N1O6</chem>	
formula weight	455.53	
temperature (K)	140(2)	
λ [Cu K α] (Å)	0.71073	
crystal system	orthorhombic	monoclinic
space group	<i>Ama</i> 2	<i>Cc</i>
unit cell dimensions		
<i>a</i> (Å)	13.8342(4)	7.8582(2)
<i>b</i> (Å)	22.8608(5)	22.8598(5)
<i>c</i> (Å)	7.8578(2)	13.8341(5)
α (°)		90.00
β (°)	90.00	90.020(3)
γ (°)		90.00
volume (Å ³)	2485.11(11)	2485.11(12)
molecules per unit cell		4
D_c (g cm ⁻³)		1.218
μ (mm ⁻¹)		0.086
$F(000)$		976
crystal size (mm)	0.212 × 0.155 × 0.078	
θ range for data collection (°)	2.94–27.5	2.94–27.0
reflections collected	10423	10415
independent reflections	2776	4766
R_{int}	0.0368	0.0332
absorption correction	none	
data/restraints/parameters	2776/1/173	4766/2/299
goodness of fit on F^2	1.059	1.737
final R indices [$I > 2\sigma(I)$]	$R_1 = 0.0413$ $wR_2 = 0.1558$	$R_1 = 0.0693$ $wR_2 = 0.0908$
R indices (all data)	$R_1 = 0.0552$ $wR_2 = 0.1970$	$R_1 = 0.0928$ $wR_2 = 0.0988$
largest diff peak/hole (e·Å ⁻³)	0.166/−0.202	0.966/−0.680

^aThe transformation from *Ama*2 to *Cc* requires a permutation of *a* and *c* axes.

unit. The quoted setup works with pulses generated by the 800 nm line of a Ti:sapphire femtosecond laser. The ultrashort laser pulse is split into the pump and probe beams and directed throughout the system of mirrors to the emitter and detector, which are both based on the low-temperature grown GaAs dipole antennas. The pump beam is focused on the biased emitter antenna to generate the THz pulses through the photoconductive phenomenon. Such pulses last near 1 ps and have a broadband spectrum, which usually covers the range of ~ 3 –100 cm⁻¹. The sample was ground using a mortar and pestle in order to reduce the particle size and avoid the scattering loss. A mixture containing 10% of the sample and 90% of high-density polyethylene (HDPE) was prepared to obtain a 400 mg pellet. A pure polyethylene sample was used as a reference. The spectrum was acquired by accumulation of 3600 scans.

Computational Details. Density functional theory (DFT) calculations in periodic boundary conditions (PBC) were carried out using the plane-wave/pseudopotential method implemented in CASTEP version 6.1.^{25,26} Exchange and correlation were defined with the Perdew–Burke–Ernzerhoff^{27,28} generalized gradient approximation (GGA) exchange-correlation functional, as well as with its revised form according to Hammer (rPBE).²⁹ Norm-conserving pseudopotentials (NCPP) were used along with the 1050 eV plane-wave kinetic energy cutoff. In order to ensure a highly reliable convergence of the low-energy phonon range, the baseline size was multiplied by a factor of 4, referring to the kinetic energy cutoff for the charge density and potential. The Monkhorst–Pack grid was kept to maintain the *k*-spacing of 0.07 Å⁻¹. The convergence criteria in variation of the total energy, maximum force, external stress, maximum displacement, and SCF iterations were defined as 1×10^{-10} eV/atom,

1×10^{-5} eV/Å, 0.0001 GPa, 1×10^{-6} Å, and 1×10^{-12} eV/atom, respectively.

The phonon frequencies were obtained by diagonalization of the dynamical matrices computed using density functional perturbation theory (DFPT).^{26,30–35} The IR/THz spectra were calculated by using the computed permittivity and Born charges tensors from which the influence of the LO-TO splitting on the absorption spectrum was probed. Raman activity tensors were obtained with the hybrid finite displacement/DFPT method in the presence of an external field³⁶ and finally transformed into Raman intensities, by taking into account the excitation line and the thermodynamic conditions.

In addition, the calculations via the molecule-in-a-box (15 × 15 × 15 Å) methodology were performed by using the above quoted numerical settings. The calculations were further supported by molecular modeling, with very tight convergence criteria defined in Gaussian 09 rev D.1,³⁷ at the PBE/6-31++G(d,p) level of theory. Such an approach allowed us to check the consistency of the plane-wave/pseudopotential approach, which is sensitive to the choice of the pseudofunctions—especially when dealing with a higher wavenumber range—as well as to probe the environment influence on the vibrational spectrum.

The molecular and crystal structures were visualized with the help of J-MOL,³⁸ Crystal Explorer,³⁹ and VESTA⁴⁰ programs.

III. RESULTS

X-ray Crystallography. The crystallographic structure of LCDP solved at 140 K is presented in Figure 1a. The system was found to crystallize in the orthorhombic *Ama*2 (C_{2v}^{16}) space group defined by the following cell parameters: *a* = 13.8342 Å; *b* = 22.8608 Å; *c* = 7.8578 Å; $\alpha = \beta = \gamma = 90^\circ$. There are four molecules equivalent by symmetry in the conventional unit cell. The asymmetric unit consists of one-half of a lacidipine molecule, since the four molecules in the unit cell are lying on a crystallographic mirror (site symmetry *m*, Wyckoff position *b*) and are therefore highly symmetric. The molecular symmetry in *C_s* and the mirror-plane molecular symmetry state that the (E)-4,2-[(*t*-butoxycarbonyl)vinyl]-phenyl moiety is oriented perpendicularly to the 1,4-dihydropyridine core. The symmetry elements for the *Ama*2 structure—making the four molecules of the unit cell symmetry-equivalent—include rotation and screw axes as well as a glide plane.

Nevertheless, the 0 K DFT geometry optimization—with, both molecular and periodic models—reveals that the *C_s* molecular symmetry corresponds to the saddle point on the potential energy surface (PES) of the molecule/crystal. The instability is reflected by both models with the occurrence of small-energy imaginary modes (~ 10 –15 cm⁻¹). It is therefore necessary to go deeper into the X-ray structure analysis.

The loss of the mirror on the molecular sites may give rise to different space groups than the *Ama*2 one, initially found by X-ray diffraction, such as the monoclinic *A1a1* space group, or other orthorhombic space groups with a primitive cell such as *Pnn2*.⁴¹ However, the X-ray diffraction measurements clearly indicate a face-centered lattice. Then, the only possibilities for the structure are *Ama*2 or *A1a1* (conventionally *Cc*, with *a* = 7.8578 Å; *b* = 22.8608 Å; *c* = 13.8342 Å; $\alpha = \gamma = 90^\circ$; $\beta \approx 90^\circ$).

In order to find an equilibrium geometry of both the LCDP molecule and the crystal, the mirror-plane structures were further relaxed in the direction of one of the local minima defined by the imaginary modes, and the presence of the stationary point was confirmed by subsequent vibrational analysis, which finally did not reveal any imaginary frequencies. As a consequence, the optimization breaks the mirror-plane, leading to *C₁* molecular symmetry, where the (*tert*-

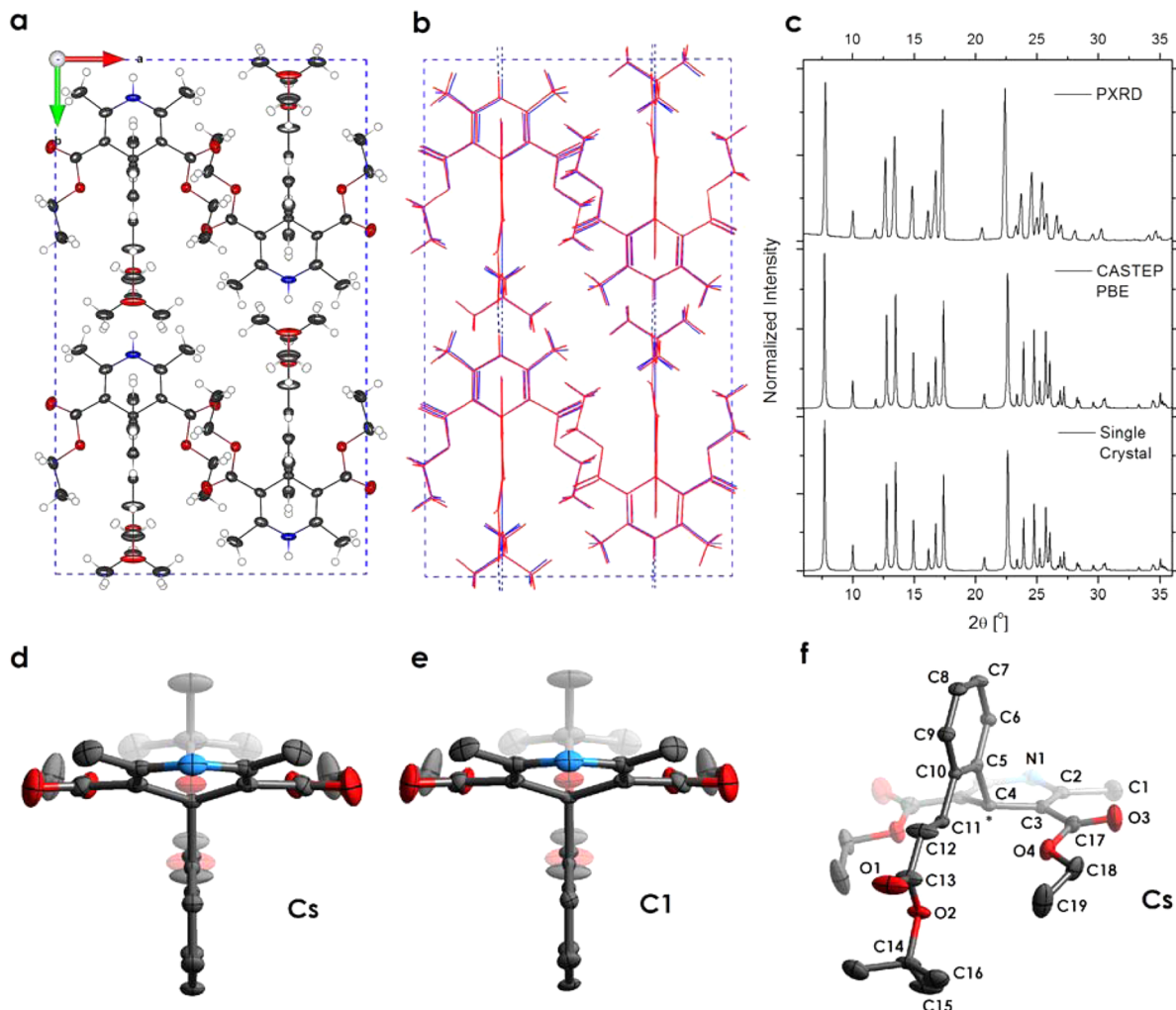


Figure 1. (a) The crystallographic structure of the lacidipine single-crystal, solved at 140 K, presented toward the *c*-axis, with the non-hydrogen thermal ellipsoids of 50% probability. (b) The superposition of the unit-cell obtained from the X-ray analysis (*Ama*2 in blue color) and the CASTEP-PBE-NCPP-1050 eV equilibrium structure (*Cc* in red color). (c) The collection of the powder XRD patterns (PXRD), presented against the theoretical patterns simulated from the single-crystal data (*Ama*2) and from theoretical PBE calculations (*Cc*). (d) Molecular view of LCDP with the atom numbering adopted in the present study. The molecule lies on a mirror passing through the N1, O1, O2, and C4–C15 atoms. (e) The molecular structure refined in the frame of *Ama*2 (*C_s*) and (f) *Cc* (*C₁*) space group.

butoxycarbonyl)vinyl conformation becomes twisted. The following of the imaginary phonon supports group theory predictions, since the Γ -point instability transforms the structure from the orthorhombic *Ama*2 down to the monoclinic *Cc* one with maintaining of the glide plane symmetry. In addition to the zone-center phonon calculations, the phonon density of states has been calculated for the set of special points in the reciprocal space (which might cover possible cell tripling). The calculations did not reveal any additional imaginary modes for any *q*-point in the Brillouin Zone. Hence, the quoted structural instability can be directly attributed to the conformational source.

As can be deduced from the anisotropic displacement parameters (ADP) (see Figure 1a), the thermal motions result in the highly symmetric structure observed at the X-ray accuracy, due to the terminal moiety flipping between two local minima on molecular PES. Such observation may suggests significant dynamics of the (*tert*-butoxycarbonyl)vinyl moiety and may somehow support the well-known photoinstability of the title compound by promoting the light-induced *trans* \rightarrow *cis* isomerization through the temperature-induced motions.

Figure 1b presents the superposition of the experimentally and theoretically (CASTEP PBE) derived crystal structures, reflecting the slight differences in the molecular conformation. By comparing Figure 1a,b, one can clearly see that the differences are smaller than the thermal displacements of atoms. The chemical purity of the polycrystalline sample—used in all the subsequent spectroscopy measurements—was examined with powder X-ray diffraction (PXRD), confirming a high quality of the studied material. The experimental PXRD spectrum was presented against the simulated patterns from both experimentally and theoretically delivered atomic coordinates (see Figure 1c). Both theoretical patterns are undistinguishable, staying in excellent agreement with the experimental powder patterns and confirming the structural identity of the single-crystal and the powder sample of pure lacidipine.

Therefore, we have also solved the structure in the *Cc* space group. There are four lacidipine molecules per unit cell, but the asymmetric unit is now the entire molecule because of the loss of the mirror symmetry. Nevertheless, the resulting *R*-factor = 4.62% was found to be slightly worse (mainly because of the

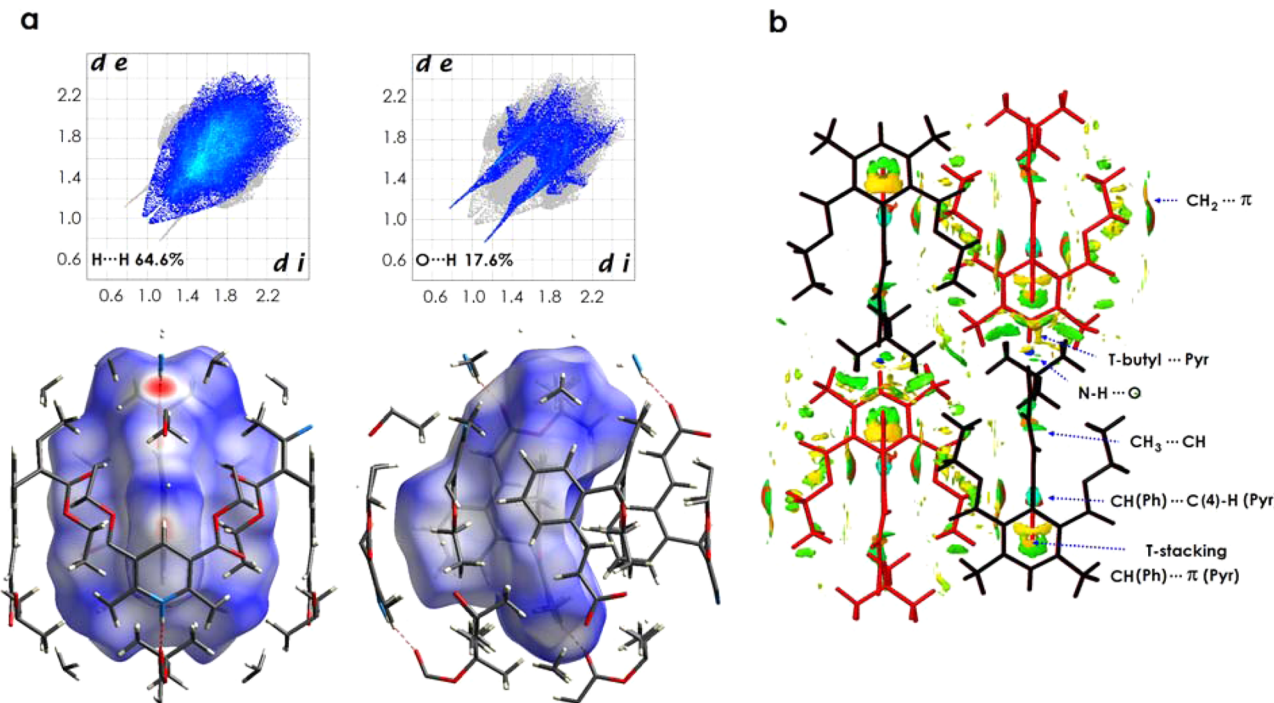


Figure 2. (a) Hirshfeld surface analysis of the intermolecular interactions in lacidipine crystal, representing the proximity of close contacts around the molecule within a network (white, distance (d) equals the van der Waals distance; blue, d exceeds the van der Waals distance; red, d is less than the van der Waals distance). The fingerprint plots present the dominating close-contacts (H···H in 64.6%; O···H in 17.6%). (b) The isosurface (0.25) of the noncovalent interactions analysis in the lacidipine unit-cell along with assignment of the most prominent interactions. The significantly attracting forces are colored in blue, whereas the repulsive interactions are shown in red. Weak van der Waals forces are marked in green and yellow, following their repulsive nature.

increase of independent Bragg reflections), and the resulting cell parameters were defined as follows: $a = 7.8541(2)$ Å; $b = 22.8562(7)$ Å; $c = 13.8324(9)$ Å; $\alpha = \gamma = 90^\circ$; $\beta = 90.020(3)^\circ$. There is no significant deviation of β from 90° to clear-cut between the two possible *Ama*2 and *Cc* space groups. The *C_s* and *C₁* molecular structures obtained from both *Ama*2 and *Cc* refinements are shown in Figure 1, panels d and e, respectively. In *Ama*2 the molecule lies on a mirror with a large ellipsoid, which indicates a lower symmetry or a disorder. For the *Cc* space group the molecular structure is still very close to the one obtained in *Ama*2, and the molecule looks symmetric with respect to a mirror but the large ellipsoids also indicate a disorder. Hence, since all bonds and angles look symmetry equivalent within the error bars of the crystallographic structure analysis, the problem cannot be solved at X-ray resolution.

In addition to X-ray diffraction, the full structural optimization of the *Cc* structure was performed with inclusion of the semiempirical dispersion corrections to PBE functional (referring to 0 K), leading to the cell parameters equal to $a = 7.7978$ Å; $b = 22.4339$ Å; $c = 13.5047$ Å; $\alpha = \gamma = 90^\circ$; $\beta = 90.8775^\circ$ and $a = 7.8055$ Å; $b = 22.7939$ Å; $c = 13.7667$ Å; $\alpha = \gamma = 90^\circ$; $\beta = 91.4489^\circ$ for PBE-D2⁴² (Grimme's D2) and PBE-TS (Tkatchenko and Scheffler) schemes,⁴³ respectively. Nevertheless, because of the practical limitations of the present linear-response implementation, all the theoretical calculations referring to the vibrational analysis were performed at the experimentally derived cell parameters.

The conventional cell can be further reduced with the use of symmetry operators down to the primitive-cell level built by two LCDP molecules, and all the subsequent calculations were performed with the reduced-size cell with full inclusion of the symmetry operators.

The molecular structure with adopted atom numbering is given in Figure 1f, where the mirror passes through the N1, O1, O2, and C4–C15 atoms. The collection of selected internal coordinates comparing the experimental (*Ama*2 structure) and calculated values is given in the Supporting Information (see Table S1).

A detailed internal coordinate analysis shows that most of the bond lengths and valence angles are predicted with excellent accuracy—better than 1.5% in most cases. Excluding the X-H coordinates—which could not be properly defined in the X-ray experiment—some deviations were found for the C=C length in the vinyl part, where the theoretical results provide a deviation of ca. 4%.

The theoretically predicted break of the mirror-plane symmetry is reflected by slight changes in the [(*tert*-butoxycarbonyl)vinyl] conformation. The most prominent differences in the torsional angles are found for the dihedral angles around the C(10)–C(11) bond, which reach 10°. The conformation of the butoxy-carbonyl part is predicted with the deviations reaching ~6°. The twisted nature of the equilibrium conformation can be attributed to the internal steric hindrance between the C(4)-H and C(11)-H fragments and may suggest that the H–C=C–H fragment avoids close contacts. Noticeable dynamics of the whole terminal part is clearly reflected by the *c*-axis anisotropy of the carbon and oxygen ADPs.

Intermolecular Interactions Analysis. In order to give some insight into the nature of weak forces stabilizing the discussed structure, intermolecular interactions were analyzed based on the theoretically optimized ionic coordinates. The intermolecular interactions were identified with the help of the

Table 2. Energy Decomposition of the Interaction Energy between Molecular Pairs in LCDP Crystal (Cc), according to the PIXEL Approach (Given Per Molecule)^a

selected interactions	symmetry	energy decomposition ^b [kJ/mol]				
		$E_{\text{Coul.}}$	$E_{\text{Pol.}}$	$E_{\text{Disp.}}$	$E_{\text{Rep.}}$	$E_{\text{Tot.}}$
N—H···O	$-0.5 + x, 0.5 + y, z; 0.5 + x, -0.5 + y, z$	-56.4	-20.0	-22.3	69.0	-29.7
CH ₂ ···π	$-0.5 + x, 0.5 - y, -0.5 + z; 0.5 + x, 0.5 - y, 0.5 + z$	-29.2	-13.9	-55.2	73.7	-24.6
	$-0.5 + x, 0.5 - y, 0.5 + z; 0.5 + x, 0.5 - y, -0.5 + z$	-27.0	-12.4	-52.4	70.9	-21.0
C—H(Ph)···C(4)—H(Pyr)	$0.5 + x, 0.5 + y, z; -0.5 + x, -0.5 + y, z$	-12.2	-8.0	-38.0	42.6	-15.6
C—H(Ph)···π(Pyr)	$1 + x, y, z; -1 + x, y, z$	-21.4	-13.5	-50.4	71.0	-14.3
CH ₃ ···CH	$x, -y, -0.5 + z; x, -y, 0.5 + z$	-1.6	-1.2	-10.5	7.4	-5.9
T-But···Pyr	$x, 1 - y, 0.5 + z; x, 1 - y, -0.5 + z$	-6.1	-1.9	-8.5	11.9	-4.6
	lattice energy	-153.8	-68.2	-241.7	346.5	-118.9

^aThe molecular electron density was restored at the PBE-D2/6-31++G(d,p) level of theory for the coordinates taken from the full-structural optimization (CASTEP/PBE-D2). ^b $E_{\text{Coul.}}$ – Coulomb; $E_{\text{Pol.}}$ – polarization; $E_{\text{Disp.}}$ – dispersion; $E_{\text{Rep.}}$ – repulsion; $E_{\text{Tot.}}$ – total.

Hirshfeld surface^{44–48} and noncovalent interactions (NCI) analysis.⁴⁹ The results are illustrated in Figure 2.

In addition to qualitative analysis, the intermolecular energies were estimated and partitioned over the Coulombic, polarization, dispersion, and repulsion terms with the help of the PIXEL method.^{50,51} Quantitative analysis was based on the electron density recovered with Gaussian09 at the PBE-D2/6-31++G(d,p) level of theory as referring to the coordinates taken from the fully optimized CASTEP/PBE-D2 crystal structure. The results are collected in Table 2, where the most prominent intermolecular forces account more than 95% contributions to the lattice energy.

A Hirshfeld surface is a visualization tool, representing the interaction of the electron density of selected molecule with that of the surrounding crystal structure. The surface is defined around the molecule at the point where the contribution to the calculated electron density from the object and the surrounding is equal. The property projected on the surface presented here is the normalized contact distance (d_{norm}) from the surface to the nearest external atom (white, distance (d) equals the van der Waals distance; blue, d exceeds the van der Waals distance; red, d is less than the van der Waals distance). The surface was produced by the program Crystal Explorer.³⁹

Fingerprint analysis of the Hirshfeld surface, shown in Figure 2a, suggests that the H···H and O···H contacts dominate the crystal interactions. The most significant forces stabilizing the crystal structure are due to the N—H···O hydrogen bondings, propagated to infinity. The bonding comes from the 1,4-dihydropyridine cores, donating protons to the *tert*-butoxy carbonyl moieties in the neighboring molecules. Hence, the formation of the hydrogen bond restrains the dynamics of the (*tert*-butoxycarbonyl)vinyl chain. Hydrogen bonding leads to the presence of antiparallel molecular chains distributed toward the crystallographic *b*-axis. The interactions can be observed in the Hirshfeld surface as the intense red areas. Hydrogen bonding can be classified as the nonlinear bond of moderate strength, with the N—H···O angle equal to 164° and 140° according to the X-ray analysis and the theory, respectively, where the donor–acceptor distance can be estimated as ca. 2.9 Å.⁵² The PIXEL analysis confirms the moderate strength of the N—H···O forces as giving the total stabilization energy of -29.7 kJ/mol per each bond.

By analyzing Figure 2a, one can also see a bright red spot around the C(4)-bonded hydrogen which is in close contact with the C(8)-attached H atom. It suggests the existence of the so-called dihydrogen bonds (CH(Ph)···C(4)—H(Pyr)), which stabilize the crystal structure in the *c*-axis direction by linking

the 1,4-dihydropyridine moieties with the neighboring phenyl rings. The H···H distance of less than 2.4 Å, which is twice the van der Waals radius of hydrogen atom (1.2 Å), is the most widely used geometrical criterion to identify formation of dihydrogen bonds. An analysis of the crystallographic structure stays in line with such an assumption. The distance found with X-ray is 2.148 Å, while an equilibrium distance from pure GGA (PBE) equals 1.959 Å. An inclusion of the vdW corrections delivers even shorter distances of 1.925 and 1.914 Å, for the PBE-TS and PBE-D2 corrections, respectively. However, due to electrostatic nature of the dihydrogen bonding, the van der Waals cutoff criterion is nevertheless criticized, since the electrostatic interaction acts beyond this distance.^{53,54} The population analysis (CASTEP-PBE-NCPP-1050 eV), however, provides the Mulliken charges (e) of 0.24 and 0.25 for the C(4)- and C(8)-bonded hydrogens, respectively, while the calculated Hirshfeld partial charges (e) are equal to 0.02 and 0.04. Since the charges at both H atoms are similar, the discussed interactions can be classified as the van der Waals (vdW) dihydrogen bonds. The PIXEL analysis estimates their total contribution to the crystal stabilization of -15.6 kJ/mol. One should note that close packing gives a significant contribution from repulsive terms, which further compensates the dispersion terms, making the Coulombic and polarization contributions still important.

Only these two discussed types of interactions are highly localized, therefore, giving clear evidence of the Hirshfeld surface. The second visual aid, providing further insight into the weak vdW forces, is NCI analysis.⁴⁹ NCI is a visualization index based on the electron density and its derivatives, allowing for a direct identification of the noncovalent forces. In general, it originates from the analysis of the reduced density gradient (RDG) at the low densities. Differentiation between the noncovalent interactions is based on the analysis of the sign of the second density Hessian eigenvalue times the density. Such value allows one to characterize the interactions by means of the density strength and its curvature, while the results can be presented in the form of isosurfaces. Analysis of Figure 2b allows one to further identify the forces, which are difficult to define through the Hirshfeld surface analysis.

In addition to the above-discussed contacts, it can be clearly seen that other types of interactions are of great importance here. NCI analysis gives further evidence of the vdW forces, namely, the CH₂···π(Ph) and C—H(Ph)···π(Pyr) stackings, which significantly contribute to the stabilization energy according to the PIXEL analysis. One can note that the CH₂···π(Ph) stacking forces give stabilization greater than -20

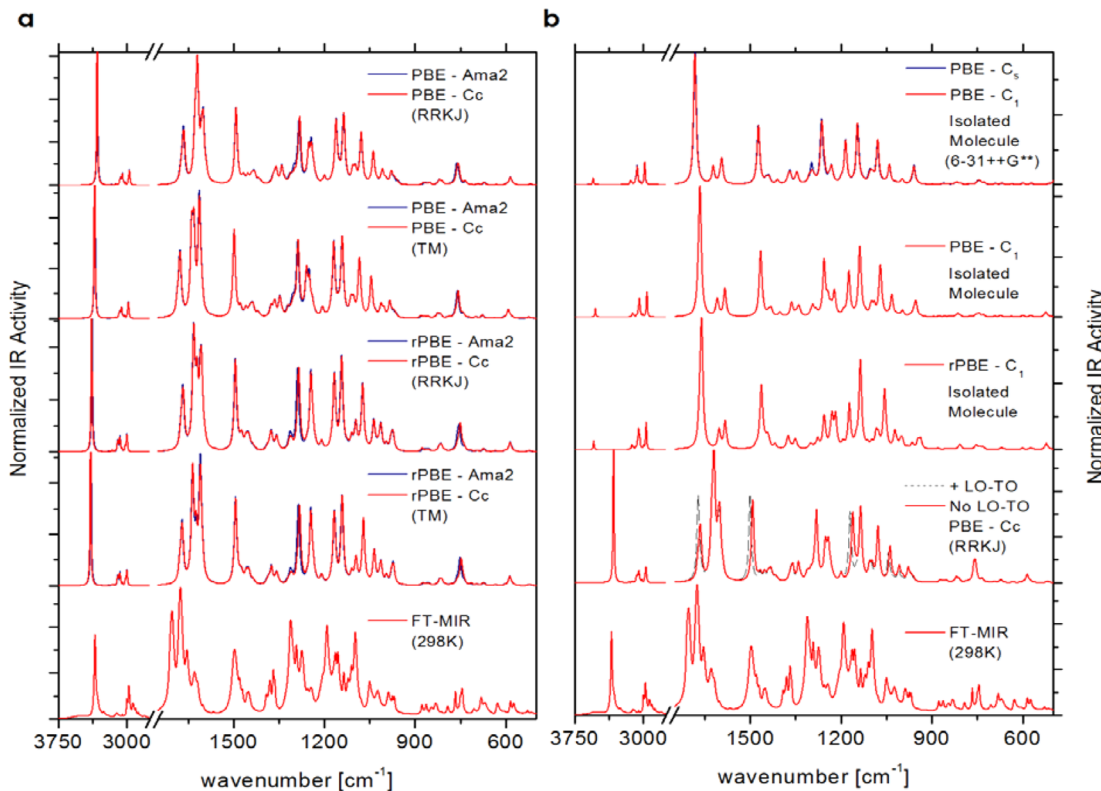


Figure 3. Experimental middle-FT-IR spectrum at 298 K along with the theoretical results (CASTEP-GGA-NCPP and G09-PBE/6-31++G**) presenting the influence of several methodological aspects on the IR response. (a) Influence of the symmetry-lowering of the crystal spectrum (*Ama*2 vs *Cc*) along with the functional (PBE vs rPBE) and pseudopotential (TM vs RRKJ) examination. (b) Influence of the long-range dipole coupling on the IR spectrum (LO-TO) against the collection of the isolated molecule calculations in the plane-wave and the fully electronic (6-31++G**) methodology.

kJ/mol for each side-chain, which in total tend to be comparable with the hydrogen bonding strength. While in the hydrogen bond case the Coulombic term is strongly dominating, the dispersion nature is of great importance for the stackings, resulting in the crystal stabilization toward the crystallographic *a*-axis.

In addition to the CH(Ph)…C(4)-H(Pyr) attractions, the crystal phase is stabilized in the *c*-axis direction by T-stacking forces, denoted here as C-H(Ph)…π(Pyr), which gives a total contribution to the lattice energy of -14.3 kJ/mol.

Finally, some weak interactions, affecting the CH₃ groups were also noticed (CH₃…CH; *t*-butyl…Pyr). The weak-strength of these forces—approximated with a limited accuracy of the quantitative analysis as ca. ~5 kJ/mol—can be rather easily reached by the thermal contributions, leading to considerable dynamics of the terminal chain.

Vibrational Analysis. The crystal structure implies that the title system gives rise to 396 zone-center phonon modes. The *Ama*2 space group (*C*_{2v}¹⁶) imposes the distribution of the symmetry species as follows: $\Gamma_{C_2v}^{16} = 111A_1 + 87A_2 + 87B_1 + 111B_2$. All vibrations are in principle able to be observed with both IR and Raman spectroscopy, since the structure is not centrosymmetric. Nevertheless, the reduction of the symmetry down to *Cc* (*C*_s⁴) results in the following distribution of the Γ -point vibrations: $\Gamma_{C_s}^4 = 198A' + 198A''$.

The influence of the symmetry-lowering on the vibrational spectrum of LCDP crystal has been probed theoretically and reported in Figure 3a (*Ama*2 vs *Cc*) with an example of the middle-IR spectrum (which has been analyzed in more detail further on). According to the figure, one cannot find any

noticeable differences, which suggests that the effect is very subtle and does not significantly affect the vibrational dynamics of the internal modes.

In addition to the influence of symmetry-lowering, we have tried to standardize the linear-response DFT computations. Since the convergence of the plane-wave calculations depends on several factors, it is interesting to note some of the methodological aspects. Recently, we have shown that the linear-response approach can be extremely successful in simulations of both optical and inelastic neutron scattering spectra of the hydrogen-bonded systems and large molecular crystals.^{55,56}

In general, the applied methodology refers to the non-fully electronic description of the molecular moieties as using the combination of plane-waves and pseudopotentials. The selection of pseudofunctions may give some error contributions, especially when referring to the higher-wavenumber range, which is due to large-amplitude displacements. Since the linear-response methodology actually limits the use of pseudopotentials to the norm-conserving (NCPP) ones, we have tested their influence by employing the NCPPs generated using two different pseudization schemes, namely, the Troullier-Martins (TM)⁵⁷ and Rappe-Rabe-Kaxiras-Joannopoulos (RRKJ) approach.^{58,59} Some slight differences in the intensity relations were noticed in the wavenumber range greater than 1500 cm⁻¹, making the RRKJ selection favorable. An influence of the basis set was also examined by analyzing the PBE/RRKJ calculations (CASTEP), performed via the isolated molecule-in-a-box methodology, against the full-electronic results delivered by the PBE/6-31++G(d,p) level of theory

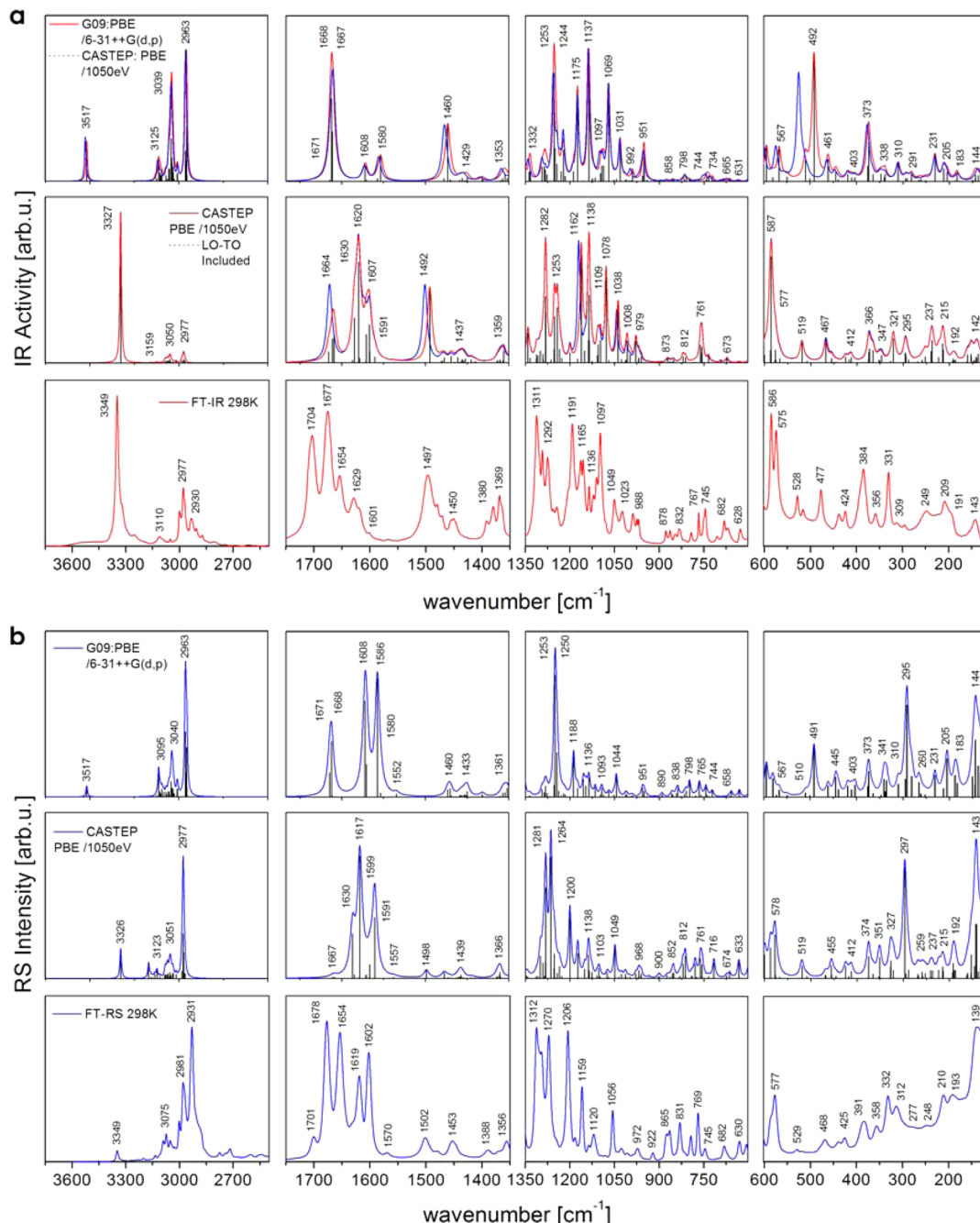


Figure 4. Collection of experimental and theoretical IR (a) and Raman (b) spectra in the range of 3750–120 cm^{-1} . The CASTEP calculations refer to the PBE/RRKJ-1050eV level of theory, while the G09 calculations correspond to PBE/6-31++G**. The G09 wavenumbers were divided by the factor of 1.0095, while the remaining wavenumbers are left unscaled.

(Gaussian09). We have already found some systematic wavenumber underestimation in the solid-state calculations (PBE/RRKJ) for other hydrogen-bonded systems.^{55,60} According to Figure 3b, there is in fact no differences in the IR intensity relations in both isolated-molecule models. A detailed analysis revealed that there is a linear relation between the calculated wavenumbers defined as PBE/6-31++G(d,p) = $1.00905 \times$ PBE/RRKJ-1050eV ($R^2 = 0.9994$). In addition, we have illustrated the functional influence by using standard PBE^{27,28} along with its “hard” rPBE revision (see Figure 3),²⁹ since the latter one has been proven to be promising in the vibrational analysis of hydrogen-bonded solids.

Finally, the vibrational frequencies in both infrared and Raman spectra can be affected by a coupling of phonon modes with a macroscopic electric field. In such a case, an infrared active mode has an associated dipole moment, which changes the spectrum in the presence of a long-range dipole–dipole coupling. Such coupling manifests itself in a frequency difference between the longitudinal and transverse optical modes, which is known as LO-TO splitting.⁶⁰ The effect was examined by including the nonanalytical contribution based on the calculated Born charges and the calculated dielectric tensor. The computations, however, reveal only a very slight influence of the long-range dipole coupling, indicating that the system is nonpolar.

Table 3. Collection of the Experimentally Observed FT-IR and FT-RS Wavenumbers for Pure Lacidipine [cm^{-1}] along with a Tentative Band Assignment^a

experiment		crystal	isolated molecule			tentative band assignment
IR [cm^{-1}]	RS [cm^{-1}]	CASTEP [cm^{-1}]	CASTEP [cm^{-1}]	G09 [cm^{-1}]		
3349 st	3349 vw	3326.6[A'']; 3326.2[A']	3524.8	3517.0	$\nu\text{N}-\text{H}$	
3110 vw		3158.7[A'']; 3158.7[A']	3131.1	3124.7	$\nu\text{H}-\text{C}=\text{C}-\text{H}$	
2977 m		3050.2[A'']; 3050.0[A']	3043.9	3038.7	νCH_3 (Trt); νCH_3 (alkyl)	
2930 w	2931 w	2976.7[A']; 2976.5[A'']	2960.3	2962.7	$\nu^{ss}\text{CH}_3$ (R_1)	
1704 vst	1701 w	1673.4[A'']	1672.0	1671.4	$\nu\text{C}=\text{O}$ in-phase (alkyl); νCCR_1	
		1666.6[A']			$\nu\text{C}=\text{O}$ (alkyl); $\beta\text{N}-\text{H}\cdots\text{O}$; νCCR_1	
		1663.5[A']			$\nu\text{C}=\text{O}$ (alkyl); $\beta\text{N}-\text{H}\cdots\text{O}$; νCCR_1	
		1661.9[A'']	1667.3	1666.6	$\nu\text{C}=\text{O}$ out-of-phase (alkyl); $\beta\text{N}-\text{H}\cdots\text{O}$; νCCR_1	
1677 max	1678 max	1630.5[A']; 1627.0[A'']	1664.9	1668.2	$\nu\text{C}=\text{O}$ (Trt); $\nu\text{C}=\text{O}$ out-of-phase (alkyl); νCCR_1	
1654 st	1654 vst	1619.6[A'']; 1617.3[A']	1609.2	1608.0	$\nu\text{C}=\text{O}$ (Trt); $\nu\text{HC}=\text{CH}$; $\nu\text{C}=\text{O}$ in-phase (alkyl); νCCR_1	
1629 m	1630 m	1606.2[A'']; 1605.7[A']	1604.9	1605.1	$\beta\text{N}-\text{H}\cdots\text{O}$	
1617 m	1619 st	1600.4[A'']; 1599.3[A']	1583.6	1585.7	$\nu\text{HC}=\text{CH}$; $\nu\text{C}=\text{O}$ (Trt); νCCR_2	
1601 w	1602 vst	1590.7[A'']; 1590.5[A']	1583.9	1580.0	$\nu\text{HC}=\text{CH}$; νCCR_2	
1497 st	1502 w	1497.8[A'']; 1491.9[A']	1465.6	1459.6	$\beta\text{N}-\text{H}\cdots\text{O}$; νCCR_1	
		1439.3[A']'; 1439.2[A']	1433.6	1433.3	δCH_3 (Trt); $\delta\text{CH}_2-\text{CH}_3$; δCH_3 (R_1)	
1450 w		1436.8[A']'; 1436.1[A'']	1437.2	1428.6	δCH_3 (Trt); $\delta\text{CH}_2-\text{CH}_3$; δCH_3 (R_1); $\delta\text{R}_2-\text{H}$	
1311 vst	1312 m	1281.6[A'']; 1281.4[A']	1256.4	1253.0	$\delta\text{C}=\text{C}-\text{H}$; $\nu\text{C}(\text{vinyl})-\text{C}(\text{ester})$	
	1295 m	1263.9[A']'; 1263.7[A'']	1254.4	1249.6	$\nu\text{R}_2-\text{C}=\text{C}$; $\delta\text{C}=\text{C}-\text{H}$; $\delta\text{R}_2-\text{H}$	
1292 st		1253.3[A'']'; 1252.9[A']	1246.1	1243.6	τCH_2 ; $\delta\text{C}=\text{C}-\text{H}$	
1244 w	1243 vw	1234.9[A'']; 1234.9[A']	1222.5	1221.1	$\nu\text{C}-\text{C}(\text{Trt})$; $\delta\text{C}=\text{C}-\text{H}$	
1205 m	1206 m	1199.9[A'']; 1199.9[A']	1191.6	1187.7	$\delta\text{R}_2-\text{H}$; $\nu\text{R}_2-\text{C}=\text{C}$; $\delta\text{C}=\text{C}-\text{H}$	
1191 st	1184 vw	1173.4[A'']'; 1161.7[A']	1174.4	1174.6	$\gamma\text{C}(4)-\text{H}$	
		1150.6[A']'; 1150.4[A'']	1153.4	1145.8	$\delta\text{R}_2-\text{H}$	
1097 st		1078.3[A'']'; 1074.6[A']	1070.8	1069.4	$\beta_1\text{R}_1$; $\nu\text{C}-\text{O}(\text{ester})$	
	1056 w	1048.8[A'']'; 1048.7[A']	1047.1	1044.0	$\beta_3\text{R}_2$	
1049 m		1038.4[A'']'; 1036.0[A'']	1032.7	1031.3	$\nu\text{CH}_2-\text{O}$	
586 w	586 vw	587.2[A'']'; 585.8[A'']	524.6	491.5	$\delta\text{C}-\text{N}-\text{C}(\text{R}_1)$; $\delta\text{C}=\text{C}-\text{O}$	
575 w	577 w	577.8[A'']'; 576.6[A'']	574.0	566.6	$\delta\text{C}-\text{N}-\text{C}(\text{R}_1)$; $\delta\text{C}=\text{C}-\text{O}$	
528 vw	529 vw	519.3[A'']'; 519.2[A'']	513.9	509.5	$\delta\text{C}=\text{C}-\text{C}$; $\delta_{sb}\text{Trt}$	
477 vw	478 vw	468.6[A'']'; 467.4[A']	464.2	461.2	$T_3\text{R}_2$; <i>wester</i> (Trt)	
395 w	391 vw	374.4[A'']'; 373.1[A']	379.7	373.4	$\delta_{sb}\text{Trt}$; $\delta\text{C}-\text{C}-\text{CH}_3(\text{R}_1)$; $\delta\text{CH}_3-\text{C}-\text{O}$; $\delta\text{C}=\text{C}-\text{O}$	
384 w	373 vw	365.6[A'']'; 365.4[A']	365.5	364.0	$\delta_{sb}\text{Trt}$; $\delta\text{C}-\text{C}-\text{CH}_3(\text{R}_1)$; $\delta\text{CH}_3-\text{C}-\text{O}$; $\delta\text{C}=\text{C}-\text{O}$	
312 w		296.8[A'']'; 295.9[A'']	294.8	294.5	$\delta\text{C}-\text{C}-\text{CH}_3(\text{R}_1)$; $\nu\text{C}(\text{vinyl})\text{H}\cdots\text{H}-\text{C}(4)$	

^aThe experimental data are presented against the computationally results obtained both in the plane-wave (CASTEP: Crystal/Isolated Molecule PBE/RRKJ-1050 eV) and full-electronic (G09: Isolated Molecule PBE/6-31++G**) methodologies. The phonon symmetry is denoted in a bracket [A'; A''] for each pair of the symmetry-related vibrations, which their theoretically estimated IR and RS intensities (A^{IR} ; I^{RS}). The G09 wavenumbers were divided by the factor of 1.0095, while the remaining wavenumbers are left unscaled. Table legend: vw, w, m, st, vst, max—relative experimental intensity (vw < 10%; w > 10%; m > 25%; st > 50%; vst > 75%; max = 100%). alkyl – $\text{COOCH}_2\text{CH}_3$; R_1 – 1,4-dihydropyridine; R_2 – phenyl ring; Trt – refers to the (*tert*-butoxycarbonyl)vinyl moiety; C(4) – dihydropyridine carbon C(4); ν – stretching; δ – in-plane bending; γ – out-of-plane bending; τ – torsion; β_1 ; β_2 ; β_3 – phenyl ring in-plane deformation type 1–3; T_1 ; T_2 ; T_3 – phenyl ring out-of-plane deformation type 1–3.

Figure 3b presents an advantage of imposing the periodic boundary conditions as the intermolecular interactions clearly affect the vibrational spectrum. Hence, detailed analysis of the vibrational spectra was further based on the PBE/RRKJ-1050eV level of theory.

There are in fact no literature reports referring to the vibrational spectra of LCDP, which calls for a report of the reference spectral data. The experimental IR and Raman spectra of pure LCDP are given in Figure 4, panels a and b, respectively, along with the results delivered by both the molecular and crystal-phase harmonic calculations. In order to facilitate the discussion, the vibrational spectra were divided into several wavenumber ranges. It can be clearly seen that the isolated-molecule model is insufficient for description of both IR and Raman spectra, while the PBC calculations provide sufficient agreement between the experiment and theory, allowing for a possibly precise assignment of the spectral

features. It is also interesting to look at how the crystal environment affects the vibrational dynamics of LCDP molecule.

A detailed assignment of the most-prominent bands is given in Table 3 (see Table S2 in Supporting Information for the full collection of vibrational spectroscopy data) as referring to the internal vibrations.

3500–1750 cm^{-1} . A well-resolved single band due to the $\nu\text{N}-\text{H}$ stretching is found in the FT-IR (intense) and FT-RS (very weak) spectra at 3349 cm^{-1} as being attributed to the A'' and A' symmetry species, respectively. Despite the quasi-harmonic approximation, the quoted modes are predicted with a reasonable agreement by solid-state GGA calculations—thanks to the lucky cancellation of errors, previously revealed by Balan et al.⁶¹ According to the isolated-molecule computations, the band shifts toward lower wavenumbers for ca. 200 cm^{-1} due to the hydrogen-bond formation. According

to the empirical correlation between the vibration redshift and hydrogen bond strength proposed by Rozenberg et al.,⁶² such a value is typical for moderate-strength bonds with enthalpy of ca. 25 kJ/mol, which stays in line with the above quoted PIXEL analysis.

The experimentally observed band shape indicates that there is no further specific effects related to the H-bonding, i.e., Fermi resonance, or quasi Franck–Condon progression; hence, it can be concluded that the hydrogen bonds are not coupled to each other since one can only find noticeable growth of the intensity and the wavenumber shift. The weak features observed and predicted around 3100 cm⁻¹ can be clearly assigned to the set of ν C–H stretchings in the phenyl rings, while the ν CH₃ vibrations cover the range around 3000 cm⁻¹.

1750–1350 cm⁻¹. The complex structure of LCDP—along with the presence of specific interactions—manifests itself in a rich vibrational spectrum covering the discussed range. Since the errors due to anharmonicity are canceled out to a greater extent in solid-state GGA calculations,⁶¹ one can also expect a similar underestimation of the calculated wavenumbers for other stretching modes. Such an effect has been already reported elsewhere.^{60,63} Indeed, it has been observed here that the computed wavenumbers are systematically underestimated for ~2%, which makes the assignment of strongly overlapping bands more challenging, especially if taking into account a highly coupled nature of the related phonons. Nevertheless, the combination of the theoretical calculations with complementary optical vibrational spectra gives a chance for a possibly full interpretation.

In principle, the isolated molecule calculations suggest the existence of three well-separated bands manifested by eight normal-mode vibrations. While the highest wavenumber band corresponds to the nearly degenerated ν C=O vibrations, the lower bands are due to the coupled ν C=C vibrations of the 1,4-dihydropyridine moiety, the phenyl ring and the vinyl part. While the isolated molecule calculations do not correlate properly with the experimental features, the further support can be given by employing crystal-phase calculations which predict an existence of 16 phonon vibrations.

The experimental band observed at 1704 and 1701 with FT-IR (strong) and FT-RS (very weak), respectively, corresponds to the set of four ν C=O vibrations, predicted by the theory at 1673, 1667, 1664, and 1662 cm⁻¹. While engaging the side-chain C=O stretchings, the quoted modes are strongly coupled to the in-plane bending (β N–H···O) of the hydrogen bond along with the ν C=C stretchings within the 1,4-dihydropyridine ring. As has been presented in Figure 4, the calculations also suggests a small LO-TO splitting which claims a small difference in the experimental IR and RS wavenumbers.

An intense feature found in the IR and RS spectra at 1677 and 1678 cm⁻¹, respectively, and predicted by theory at ca. 1630 cm⁻¹ has a dual nature. While engaging the hydrogen-bonded C=O stretching, which tends to give an intense IR response, the vibration is strongly coupled to the vinyl stretching (ν HC=CH), which tends to give strong Raman signal. When referring to the isolated-molecule calculations, one can find a downward shift of ca. 30 cm⁻¹ upon formation of the N–H···O bonding. Similarly, the band found experimentally at 1654 cm⁻¹ and predicted at 1620 cm⁻¹ is of a similar nature with a dominating ν HC=CH contribution, which claims its lower intensity in the IR spectrum. According to the calculations, formation of the hydrogen bonding results in a

slight (~10 cm⁻¹) upward shift of the related wavenumbers due to strengthening of the C=C bond.

Two overlapping features can also be found in both spectra at ~1630 and 1620 cm⁻¹, being underestimated by the theory by ca. ~20 cm⁻¹. The upper band is due to the in-plane β N–H···O bending, while the lower one can be assigned to the vinyl stretching ν HC=CH coupled to the hydrogen-bonded C=O stretching and the in-plane deformation of the phenyl. Similarly, an intense band, found in the FT-RS spectrum at 1602 cm⁻¹ and barely detectable with IR spectroscopy (very weak sideband at 1601 cm⁻¹) is due to the coupled stretchings of the phenyl-vinyl moiety. Finally, an extremely weak band, found around 1570 cm⁻¹ in both experimental spectra, can be assigned to the ν CCR₂ phenyl stretchings.

A nearly pure β N–H···O bending is manifested as a weak (FT-RS) and medium-intensity band (FT-IR) around 1500 cm⁻¹. The quoted modes are predicted with excellent agreement by solid-state DFT. While the isolated molecule calculations predict the vibration at 1460 cm⁻¹, it undergoes an upward shift of ~30 cm⁻¹ upon inclusion of the crystal environment and further splits into the A'' and A' symmetry species, differing in energy in ca. 5 cm⁻¹.

The range of ca. ~1500–1350 cm⁻¹ is generally covered by the scissoring deformations of CH₂ and CH₃ groups, where the latter ones undergo “umbrella”-like symmetric bendings at lower wavenumbers.

1350–900 cm⁻¹. A complex feature with the maxima around 1310 and 1295 cm⁻¹ was found in the IR and Raman spectra. The upper band is due to the coupled ν C–C/ δ CCH vibrations within the (*tert*-butoxycarbonyl)vinyl moiety, while the lower mode is mainly attributed to the methylene twisting modes. The ν C–C stretchings in the *tert*-butyl fragment give weak spectral contributions around 1240 cm⁻¹.

While the well-separated Raman band at 1205 cm⁻¹ can be clearly assigned to the δ CCH deformations, an intense band found at 1191 cm⁻¹ has an interesting nature as being assigned to the γ C(4)–H modes. Since the mode is characterized by a large amplitude of motion and induces the intermolecular C(4)–H···O interactions, it gives a prominent IR response. According to theoretical calculations, the mode is shifted downward if turning from the isolated molecule to the crystal model. Hence it may reflect the earlier discussed CH(Ph)···H–C(4)(Pyr) interactions. Interestingly, according to Figure 4, one may note that the mode gives rise to the long-range dipole coupling as being slightly shifted upon inclusion of the LO-TO splitting term.

The rocking vibrations of the CH₂ and CH₃ groups contribute to the vibrational spectrum down to ~800 cm⁻¹, being, however, clearly mixed with other types of vibrations, that is, mainly with ν C–O stretchings and ring deformations. The quoted range has been predicted by solid-state DFT with good accuracy. One can note that the trigonal deformation of the 1,4-dihydropyridine ring, coupled to the ν C–O stretchings, gives an intense contribution to the IR spectrum at ~1097 cm⁻¹. The in-plane (β) ring deformations contribute at higher wavenumbers, while the torsional deformations (T) are predicted below ~970 cm⁻¹.

900–120 cm⁻¹. The solid-state calculations predict the large-amplitude out-of-plane deformations of the γ N–H···O bridge spread over the range ~760–715 cm⁻¹, which result in a complex feature observed in both experiments at 770 and 745 cm⁻¹, respectively. These vibrations are also coupled to the out-of-plane ester motions. It is difficult to assign the related

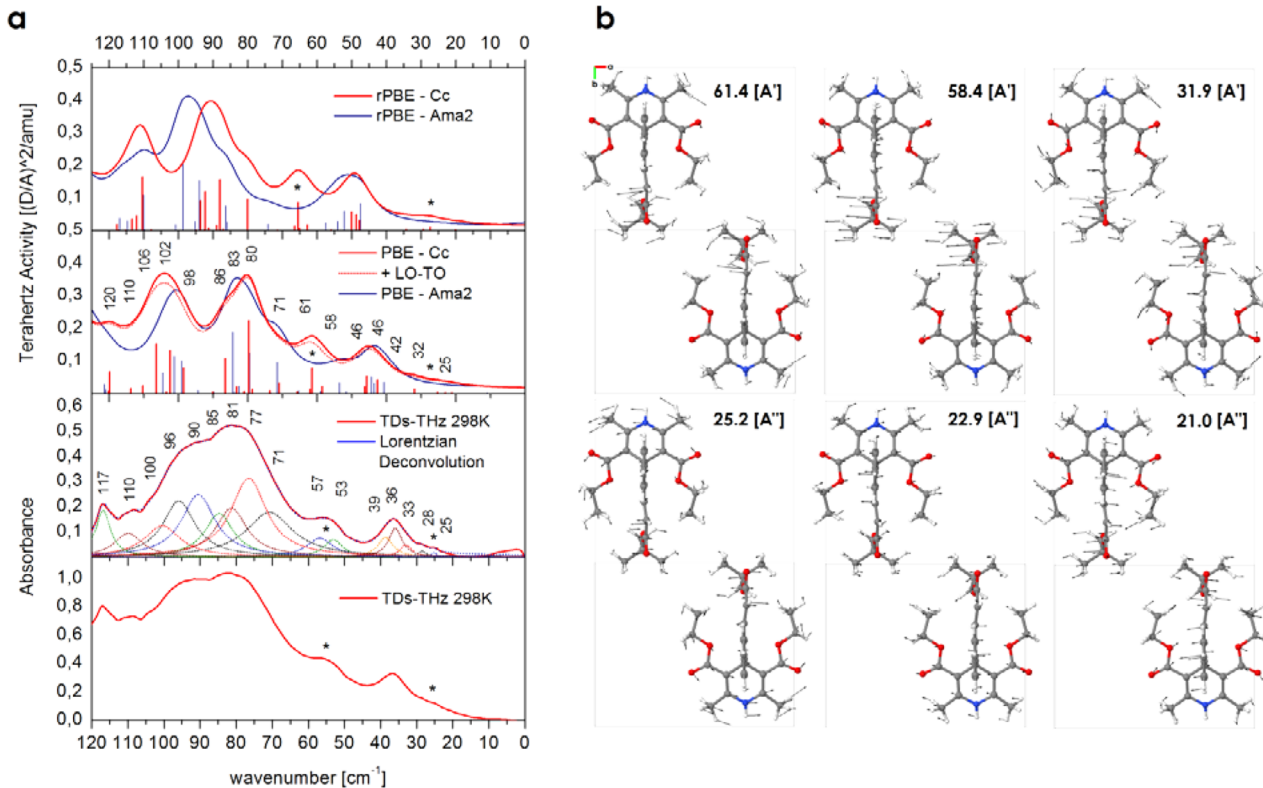


Figure 5. (a) The collection of experimental (TDs-THz) and theoretical solid-state (PBE/rPBE-RRKJ-1050 eV) terahertz spectra of pure lacidipine. The experimental spectrum was deconvoluted with the set of Lorentzian functions. The theoretical spectra are presented for both *Ama2* and *Cc* periodic models. An influence of the long-range dipole coupling is denoted as LO-TO. The absorption bands due to the “crankshaft”-type motions are denoted with an asterisk. Note that the theoretical spectra are presented in a slightly broadened scale. (b) The visualization of characteristic terahertz vibrations of the *Cc* structure (in the primitive cell projection), contributing to the experimental bands observed around ~ 30 and 55 cm^{-1} .

isolated molecule vibrations, since—according to the eigenvectors—the mode character has been substantially changed. While the $\gamma\text{N-H}$ coordinate contributes to the isolated-molecule vibration predicted at ca. 640 and 580 cm^{-1} , the nature of the coordinates contributing to the phonon modes remains the ones predicted by molecular modeling at around 700 cm^{-1} . However, one can see that a kind of potential energy distribution transfer upon formation of the hydrogen bond shifts upward the $\gamma\text{N-H}$ energy for over 150 cm^{-1} .

Similarly, a characteristic double band was observed by each spectroscopy measurement with maxima at ~ 585 and 575 cm^{-1} . These modes were predicted by the solid-state theory with excellent accuracy, being assigned to the large-amplitude $\delta\text{C-N(1)-C}$ deformation, highly affecting the $\text{N}\cdots\text{O}$ distance and being further coupled to the bending of the hydrogen-bonded $\delta\text{C-C=O}$ part. The isolated molecule calculations predict the mode to be dominated by the $\gamma\text{N-H}$ motion, where it is interesting to note a striking different wavenumbers delivered by the plane-wave (525 cm^{-1}) and full-electronic calculations (492 cm^{-1}).

The range below 550 cm^{-1} is covered by highly delocalized bending modes with large-amplitude scissoring deformations of the *tert*-butyl part. This range is predicted by the theoretical calculations with an excellent overall accuracy. However, both, the isolated molecule and periodic calculations provide a noticeable discrepancy in description of the Raman band found experimentally at 312 cm^{-1} . Both models predict its highly overestimated intensity. The vibration involves the $\delta\text{C(3)-C(2)-CH}_3$ bendings along with the motion inducing the $\text{C(vinyl)H}\cdots\text{H-C(4)}$ contacts. It seems that such an effect

tends to be purely artificial. On the other hand, the intensity can be quenched due to the dynamics of the (*tert*-butoxycarbonyl)vinyl moiety or may indicate that the conformation of the quoted moiety is even far more twisted at higher temperatures.

The range beneath 300 cm^{-1} is generally covered by torsional deformations of both methyl groups and LCDP framework.

Low-Wavenumber Vibrations ($<120 \text{ cm}^{-1}$). The phonon vibrations manifesting in the terahertz range involve substantial contributions from both internal normal modes and the intermolecular vibrations, where the latter ones engage the molecular translations and rotations. Although the vibrations are highly harmonic by their nature, being related to very small amplitudes of motion, it is extremely difficult to properly describe the low-wavenumber range because of the numerical noise coming from the applied methodology. Thus, as we have recently shown that a very high numerical precision is needed to minimize the numerical oscillations.⁵⁵ Despite the molecular complexity and multiple deficiencies of semilocal DFT, an excellent agreement between the experiment and theory has been achieved, providing a possibly full understanding of these extremely subtle vibrational transitions.

The experimental TDs-THz spectrum of pure LCDP is presented in Figure 5a against the results delivered by highly precise first-principles calculations. The experimental spectrum was baseline-corrected and further deconvoluted using the set of Lorentzian functions, corresponding to the number of relatively intense THz absorption bands suggested by the

Table 4. Collection of Experimentally Observed TDs-THz Wavenumbers for Pure Lacidipine [cm^{-1}] along with Tentative Band Assignment^a

TDs-THz		CASTEP: PBE/RRKJ-1050 eV		
ν [cm^{-1}]	ν [cm^{-1}]	symmetry	A^{THz} [(D/A) ² /amu]	tentative band assignment
117	120.1; 119.7	[A''];[A']	0.0082; 0.0668	$\delta\text{C}(3)-\text{C}(17)-\text{O}(4)$; $\tau\text{C}(1)\text{H}_3$
110	113.7; 110.2	[A''];[A'']	0.0164; 0.0242	$\tau\text{C}(4)-\text{Ph}$; $\tau\text{C}(12)-\text{C}(13)-$
100	106.4	[A'']	0.1535	$\tau\text{C}(5)-\text{C}(10)-$; $\tau\text{O}(4)-\text{C}(18)-$; $\tau\text{C}(1)\text{H}_3$
96	103.4; 102.3	[A''];[A']	0.0051; 0.1337	$\tau\text{O}(4)-\text{C}(18)-$; $\gamma\text{C}(3)-\text{C}(4)-\text{C}(3)$; $\gamma\text{C}(2)-\text{N}(1)-\text{C}(2)$
90	98.4	[A'']	0.0790	$\tau\text{CH}_2\text{H}_3$; $\tau\text{C}(5)-\text{C}(10)-$; $\rho(1,4\text{-Pyr}) \angle a \rightarrow c$
	97.9	[A'']	0.0000	$\tau\text{C}(5)-\text{C}(10)-$; $\rho(1,4\text{-Pyr}) \angle a \rightarrow c$
	96.8	[A'']	0.0004	$\rho(1,4\text{-Pyr}) \angle a \rightarrow c$; $\tau\text{CH}_2-\text{H}_3$
85	90.0; 86.5	[A''];[A']	0.0044; 0.1089	$\tau\text{O}(4)-\text{C}(18)-$; $\tau\text{C}(1)\text{H}_3$; $\tau\text{CH}_2-\text{H}_3$
81	85.6; 83.1	[A''];[A']	0.0007; 0.0217	$\tau\text{T-butyl}$ ($\tau\text{C}(13)-\text{O}(2)-$)
	80.9	[A'']	0.0069	$\tau\text{C}(3)-\text{C}(17)$; $\tau\text{C}(1)\text{H}_3$; $\tau\text{O}(4)-\text{C}(18)-$; $\delta\text{C}(12)-\text{C}(13)-\text{O}(2)$; $\tau\text{T-butyl} \rightarrow b$
77	79.7	[A'']	0.2250	$\tau\text{C}(1)\text{H}_3$; $\tau\text{C}(3)-\text{C}(17)$; $\tau\text{C}(10)-\text{C}(11)$; $\tau\text{T-butyl}$
	79.3	[A'']	0.0001	$\tau\text{O}(4)-\text{C}(18)-$; $\tau\text{CH}_2-\text{H}_3$
	78.6; 76.2	[A''];[A'']	0.0124; 0.0009	$\tau\text{O}(4)-\text{C}(18)-$; $\tau\text{T-butyl}$; $\tau\text{C}(4)-\text{Ph}$; $\gamma\text{C}(11)-\text{C}(12)-\text{C}(13)$
	73.6	[A'']	0.0098	$\rho(1,4\text{-Pyr}) \angle a \rightarrow c$; $\omega\text{C}(4)-\text{Ph}$; $\tau\text{C}(10)-\text{C}(11)$
	72.1	[A'']	0.0001	$\delta\text{C}(12)-\text{C}(13)-\text{O}(2)$; $\tau\text{T-butyl}$; $\gamma\text{C}(17)=\text{O}(3)$; $\gamma\text{C}(13)=\text{O}(1)$
71	70.9	[A'']	0.0336	$\tau\text{O}(4)-\text{C}(18)-$; $\tau\text{T-butyl}$; $\delta\text{C}(12)-\text{C}(13)-\text{O}(2)$
	65.6	[A'']	0.0060	$\delta\text{C}(12)-\text{C}(13)-\text{O}(2)$; $\tau\text{C}(1)\text{H}_3$; $\tau\text{LCDP} \angle b \rightarrow c$
	63.6	[A'']	0.0000	$\tau\text{C}(10)-\text{C}(11)-$; $\tau\text{butyl} \rightarrow a$
57	62.0; 61.4	[A''];[A']	0.0124; 0.0778	$\tau\text{C}(10)-\text{C}(11)-$; $\text{C}(12)-\text{C}(13) \rightarrow a$ (“crankshaft”); $\tau\text{T-butyl}$; $\tau\text{C}(1)\text{H}_3$
	59.7	[A'']	0.0007	$\tau\text{C}(4)-\text{Ph}$; $\tau\text{LCDP} \angle a \rightarrow b$
53	58.4	[A'']	0.0221	
	53.5	[A'']	0.0001	$\rho(1,4\text{-Pyr}) \angle a \rightarrow c$; $\omega\text{C}(4)-\text{Ph}$; $\tau\text{C}(1)\text{H}_3$; $\tau\text{butyl} \rightarrow a$
39	46.2	[A'']	0.0214	$\rho(1,4\text{-Pyr}) \angle a \rightarrow c$; $\gamma\text{C}(11)-\text{C}(12)-\text{C}(13)$; $\tau\text{C}(1)\text{H}_3$
36	45.6	[A'']	0.0523	$\gamma\text{COOCH}_2\text{CH}_3 \rightarrow c$; $\gamma\text{Ph}-(t\text{-butoxycarbonyl})\text{vinyl} \rightarrow c$
33	42.5	[A'']	0.0423	
28	31.9	[A'']	0.0141	$\tau\text{LCDP} \angle a \rightarrow b$; $\text{C}(12)-\text{C}(13) \rightarrow a$ (“crankshaft”)
25	25.2	[A'']	0.0041	
	22.9	[A'']	0.0024	$\tau\text{C}(17)-\text{O}(4)-\text{C}(18)-\text{C}(19)$; $\omega\text{C}(4)-\text{Ph}$
	22.6	[A'']	0.0004	LCDP shearing mode $\rightarrow b$ -axis
	21.0	[A'']	0.0027	LCDP shearing mode $\rightarrow c$ -axis; $\tau\text{LCDP} \angle a \rightarrow c$
-0.0	[A'']	0		acoustic modes
-0.1	[A'']	0		
-0.1	[A'']	0		

^aThe experimental data are presented against the computationally results obtained both in the plane-wave (CASTEP: Crystal-Cc/Isolated Molecule PBE/RRKJ-1050 eV) and full-electronic (G09: Isolated Molecule PBE/6-31++G**) methodologies. The phonon symmetry is denoted in a bracket [A'; A''] for each pair of the symmetry-related vibrations, where the theoretically estimated terahertz activities (A^{THz}) are given in (D/A)²/amu.

theory. Sixteen modes were identified and analyzed in detail in Table 4.

The presented theoretical calculations were performed for both *Ama2* and *Cc* models, using the PBE functional along with its revised form (rPBE). Computations directly support the previously drawn conclusion about the crystal phase symmetry.

The upper part of the terahertz spectrum is covered by multiple overlapping bands forming a broad, intense feature, which can be decomposed into the set of modes assigned to the more localized internal rotations and highly delocalized bendings.

Calculations in the frame of the mirror-plane symmetry structure (*Ama2*) do not clarify the presence of two prominent bands, denoted with an asterisk in Figure 5. In contrast, calculations based on the *Cc* phase symmetry are in excellent agreement with the experimental data. According to Figure 5b, one can clearly see that these “missing” transitions in the *Ama2* model are directly related to the (*tert*-butoxycarbonyl)vinyl moiety dynamics, revealing the “crankshaft” type motions of the terminal chain, contributing mainly in the vibrations predicted at 25, 32, and 62 cm^{-1} .

The lowest-energy vibrations also involve a substantial translational/breaking motion of the *tert*-butyl fragments, as the terminal chain is somehow stiffened by the hydrogen bonding.

An interesting vibration is predicted at 23 cm^{-1} (A'), with, however extremely low terahertz activity. The phonon mode reflects the collective translations of the antiparallel hydrogen-bonded molecular chains. Finally, the energetically lowest transition is due to a coupled rotational (twisting)–translational motions of the molecular chains toward the *c*-axis, that is, in direction where the crystal is stabilized by weak vdW forces.

IV. CONCLUSIONS

The structural properties of lacidipine were explored by combining X-ray diffraction with theoretical calculations, providing a consistent view of the dynamically raised global symmetry of the crystal-phase. The crystallographic study reveals that the system crystallizes in a highly ordered, orthorhombic space group *Ama2*, with a substantially large atomic displacement parameters (ADP) in the molecular framework. The most prominent intermolecular interactions

were qualitatively identified with the help of Hirshfeld surface and reduced density gradient analysis and further quantitatively decomposed using PIXEL approach. The role of moderate-strength N–H···O hydrogen bonding and weak H···H dihydrogen contacts in the crystal structure stabilization has been indicated. The intermolecular interactions were correlated with the vibrational spectra in both middle- and low-wavenumber range, which were possibly fully interpreted with the help of theoretical calculations. The results of the solid-state DFPT computations remain in sufficient overall agreement with the middle-wavenumber spectra, considerably affected by anharmonicity. The same methodology provides an excellent description of the low-energy vibrational transfers in lacidipine.

By combining low-wavenumber vibrational spectroscopy with solid-state DFT calculations, we were able to go beyond the structural information delivered by X-ray diffraction and illustrate how the quoted methodology can help in revealing the structural features hidden under the thermally induced dynamics.

The theoretical vibrational analysis revealed an instability of the mirror-plane symmetry and suggests that the true stationary point on the potential energy surface (PES) corresponds to a distorted lacidipine molecule crystallizing in the monoclinic Cc structure ($\alpha = \gamma = 90^\circ$; $\beta \approx 90^\circ$). The assumption has been directly confirmed by terahertz spectroscopy study. It was clearly found that the dynamic nature of the (*tert*-butoxycarbonyl)vinyl moiety give rise to the higher space group observed experimentally. Such an approach can be a very powerful tool in revealing the subtle structural differences playing a role in a proper definition of the crystal structures in large and flexible pharmaceutical molecular crystals.

■ ASSOCIATED CONTENT

Supporting Information

Figure presenting commonly found synthetic impurities and degradation products of lacidipine. Tables showing the set of internal coordinates of lacidipine crystal found experimentally and theoretically, the full collection of IR and RS wavenumbers complex along with a tentative band assignment in the medium- and low-wavenumber range. The Supporting Information is available free of charge on the ACS Publications website at DOI: 10.1021/acs.cgd.5b00251.

■ AUTHOR INFORMATION

Corresponding Author

*E-mail: kacper.druzicki@amu.edu.pl

Notes

The authors declare no competing financial interest.

■ ACKNOWLEDGMENTS

The work has been partially financed by the National Science Centre of Poland, Grant No. 2012/05/B/ST3/03176 and has also supported in part by PL-Grid Infrastructure (Grant ID: phd2013, phd2014). K.D. acknowledges the financial support of Polish Government Plenipotentiary for JINR in Dubna (Grant No. 118-8/1069-5/2014). We are also grateful to Prof. Denis P. Kozlenko (JINR, Dubna) along with the Frank Laboratory of Neutron Physics (JINR, Dubna) for supporting the research mobility of K.D. We would like to give our appreciation to Dr. Norbert Palka (Military University of Technology, Warsaw), Ms. Halina Thiel-Pawlak (Adam Mickiewicz University, Poznan), and Prof. Edward Mikuli

(Jagiellonian University, Cracow) for providing the access to the research equipment. The FT-FIR spectrum was recorded thanks to the financial support of the European Regional Development Fund in the framework of the Polish Innovation Economy Operational Program (Contract No. POIG.02.01.00-12-023/08).

■ REFERENCES

- Micheli, D.; Collodel, A.; Semeraro, C.; Gaviragli, G.; Carpi, C. *J. Cardiovasc. Pharmacol.* **1990**, *15*, 666–675.
- Bristol, J. A., Ed. *Annual Reports in Medicinal Chemistry*; Academic Press: San Diego, 1992; Vol. 27, p 330.
- McCormack, P. L.; Wagstaff, A. J. *Drugs* **2003**, *63*, 2327–2356.
- Bernini, F.; Canavesi, M.; Bernardini, E.; Scurati, N.; Bellosta, S.; Fumagalli, R. *Br. J. Pharmacol.* **1997**, *122*, 1209–1215.
- Zhang, A.; Shuli, F.; Chen, L.; Ren, L.; Qu, S.; Zhang, Y.; Yao, L.; Yang, S. *Cell. Physiol. Biochem.* **2013**, *32*, 1040–1049.
- Krenek, P.; Salomone, S.; Kyselovic, J.; Wibo, M.; Morel, N.; Godfraind, T. *Hypertension* **2001**, *37*, 1124–1128.
- Dasgupta, A.; Jeyaseeli, L.; Dutta, N. K.; Mazumdar, K.; Karak, P.; Dastidar, S. G.; Motohashi, N.; Shiratak, Y. *In Vivo* **2007**, *21*, 847–50.
- Sadgupta, A.; Dastigar, S. G. *Indian J. Med. Res.* **2012**, *135*, 913–916.
- Tang, J.; Zhu, R.; Zhao, R.; Cheng, G.; Peng, W. *J. Pharm. Biomed. Anal.* **2008**, *47*, 923–928.
- Basalious, E. B.; Shawky, N.; Badr-Eldin, S. M. *Int. J. Pharm.* **2010**, *391*, 203–211.
- Kiwilsza, A.; Mielcarek, J.; Pajzderska, A.; Wąsicki, J. *J. Microencapsul.* **2013**, *30*, 22–27.
- Gannu, R.; Palem, C. R.; Yamsani, V. V.; Yamsani, S. K.; Yamsani, M. R. *Int. J. Pharm.* **2010**, *388*, 231–241.
- Anuradha, K.; Kumar, S. *Int. J. Pharm. Med. Res.* **2014**, *2*, 50–57.
- El Kasaby, N. A.; Elsayed, I.; Elshafeey, A. H. *Int. J. Pharm.* **2014**, *472*, 369–379.
- Eswaraiah, S.; Prasada Raju, V. V. N. K. V.; Srinivas Reddy, N.; Ravindra, V. Process for Preparing Lacidipine. U.S. Patent 0043088 A1, February 22, 2007.
- Prasada Raju, V. V. N. K. V.; Reddy, G. M.; Ravindra, V.; Mathad, V. T.; Dubey, P. K.; Reddy, P. P. *Synth. Commun.* **2009**, *39*, 2137–2145.
- Mukharya, A.; Patel, P. U.; Chaudhary, S. *Int. J. Pharm. Sci. Nano.* **2013**, *6*, 2022–2032.
- Semeraro, C.; Micheli, D.; Pieraccioli, D.; Gaviragli, G.; Borthwick, A. D. GB Patent 2,164,336, 1986; *Chem. Abstr.* **1986**, *105*, 97322.
- De Filippis, P.; Bovina, E.; Da Ros, L.; Fiori, J.; Cavrini, V. *J. Pharm. Biomed. Anal.* **2002**, *27*, 803–812.
- Simonic, I.; Zupancic, S.; Golobic, A.; Golic, L.; Stanovnik, B. *Acta Chim. Slov.* **2008**, *55*, 458–461.
- McIntosh, A. I.; Yang, B.; Goldup, S. M.; Watkinson, M.; Donnan, R. S. *Chem. Soc. Rev.* **2012**, *41*, 2072–2082.
- CrysAlis RED (Version 1.171.37.31); Oxford Diffraction Ltd., 2014.
- Altomare, A.; Burla, M. C.; Camalli, M.; Cascarano, G.; Giacovazzo, C.; Guagliardi, A.; Molterni, A. G. G.; Polidori, G.; Spagna, R. *J. Appl. Crystallogr.* **1998**, *31*, 74–77.
- SHELX-97; Sheldrick, G. M. University of Göttingen: Germany, 1997.
- Clark, S. J.; Segall, M. D.; Pickard, C. J.; Hasnip, P. J.; Probert, M. J.; Refson, K.; Payne, M. C. Z. *Kristallogr.* **2005**, *220*, 567–570.
- Refson, K.; Clark, S. J.; Tulip, P. R. *Phys. Rev. B* **2006**, *73*, 155114–155136.
- Perdew, J. P.; Burke, K.; Wang, Y. *Phys. Rev. B* **1996**, *54*, 16533–16539.
- Perdew, J. P.; Burke, K.; Ernzerhof, M. *Phys. Rev. Lett.* **1996**, *77*, 3865–3368.
- Hammer, B.; Hansen, L. B.; Nørskov, J. K. *Phys. Rev. B* **1999**, *59*, 7413–7421.

- (30) Baroni, S.; Giannozzi, P.; Testa, A. *Phys. Rev. Lett.* **1987**, *58*, 1861–1864.
- (31) Gonze, X.; Allan, D. C.; Teter, M. P. *Phys. Rev. Lett.* **1994**, *68*, 3603–3606.
- (32) Gonze, X. *Phys. Rev. A* **1995**, *52*, 1086–1095.
- (33) Gonze, X. *Phys. Rev. A* **1995**, *52*, 1096–1114.
- (34) Gonze, X. *Phys. Rev. B* **1997**, *55*, 10337–10354.
- (35) Baroni, S.; Dal Corso, A.; de Gironcoli, S.; Giannozzi, P. *Rev. Mod. Phys.* **2001**, *73*, S15–S61.
- (36) Milman, V.; Perlov, A.; Refson, K.; Clark, S. J.; Gavartin, J.; Winkler, B. *J. Phys.: Condens. Matter.* **2009**, *21*, 485404–485416.
- (37) Frisch, M. J. et al. *Gaussian 09*, Revision D.1; Gaussian, Inc.; Wallingford CT, 2009.
- (38) Hanson, R. M. *J. Appl. Crystallogr.* **2010**, *43*, 1250–1260.
- (39) *Crystal Explorer*, Version 3.1; Wolff, S. K.; Grimwood, D. J.; McKinnon, J. J.; Turner, M. J.; Jayatilaka, D.; Spackman, M. A. University of Western Australia, 2012.
- (40) Momma, K.; Izumi, F. *J. Appl. Crystallogr.* **2011**, *44*, 1272–1276.
- (41) Wilson, A. J. C. *International Tables for X-ray Crystallography*; Kluwer Academic Publishers: Dordrecht, 1992, Vol. C.
- (42) Grimm, S. *J. Comput. Chem.* **2006**, *27*, 1787–1799.
- (43) Tkatchenko, A.; Scheffler, M. *Phys. Rev. Lett.* **2009**, *102*, 073005–073009.
- (44) McKinnon, J. J.; Mitchell, A. S.; Spackman, M. A. *Chem.—Eur. J.* **1998**, *4*, 2136–2141.
- (45) Spackman, M. A.; McKinnon, J. J. *CrystEngComm* **2002**, *4*, 378–392.
- (46) McKinnon, J. J.; Spackman, M. A.; Mitchell, A. S. *Acta Crystallogr. B* **2004**, *60*, 627–668.
- (47) McKinnon, J. J.; Jayatilaka, D.; Spackman, M. A. *Chem. Commun.* **2007**, 3814–3816.
- (48) Spackman, M. A.; Jayatilaka, D. Hirshfeld Surface Analysis. *CrystEngComm* **2009**, *11*, 19–32.
- (49) Johnson, E. R.; Keinan, S.; Mori-Sánchez, P.; Contreras-García, J.; Cohen, A. J.; Yang, W. *J. Am. Chem. Soc.* **2010**, *132*, 6498–6506.
- (50) Gavezzotti, A. *J. Phys. Chem. B* **2003**, *107*, 2344–2353.
- (51) Gavezzotti, A. *Mol. Phys.* **2008**, *106*, 1473–1485.
- (52) Steiner, T. *Angew. Chem., Int. Ed.* **2002**, *41*, 48–76.
- (53) Chandra Singh, P.; Naresh Patwari, G. *Chem. Phys. Lett.* **2006**, *419*, 265–268.
- (54) Desiraju, G. R.; Steiner, T. *The Weak Hydrogen Bond in Structural Chemistry and Biology*; Oxford University Press: New York, 1999.
- (55) Drużbicki, K.; Mikuli, E.; Palka, N.; Zalewski, S.; Ossowska-Chruściel, M. D. *J. Phys. Chem. B* **2015**, *119*, 1681–1695.
- (56) Drużbicki, K.; Kocot, A.; Mikuli, E.; Ossowska-Chrusciel, M. D.; Chrusciel, J. *J. Phys. Chem. B* **2012**, *116*, 11332–11343.
- (57) Troullier, N.; Martins, J. L. *Phys. Rev. B* **1991**, *43*, 1993–2006.
- (58) Rappe, A. M.; Rabe, K. M.; Kaxiras, E.; Joannopoulos, J. D. *Phys. Rev. B* **1990**, *41*, 1227–1230.
- (59) Rappe, A. M.; Rabe, K. M.; Kaxiras, E.; Joannopoulos, J. D. *Phys. Rev. B* **1991**, *44*, 13175–13175.
- (60) Łuczynska, K.; Drużbicki, K.; Lyczko, K.; Starosta, W. *Vib. Spectrosc.* **2014**, *75*, 26–38.
- (61) Balan, E.; Lazzeri, M.; Delattre, S.; Méheut, M.; Refson, K.; Winkler, B. *Phys. Chem. Miner.* **2007**, *34*, 621–625.
- (62) Rozenberg, M.; Loewenschuss, A.; Marcus, Y. *Phys. Chem. Chem. Phys.* **2000**, *2*, 2699–2702.
- (63) Górska, N.; Szostak, E.; Drużbicki, K.; Mikuli, E.; Inaba, A.; Hirao, Y. *J. Coord. Chem.* **2014**, *67*, 3135–3154.